RSC Advances

# Nanostructured hexahedron of bismuth ferrite clusters: Delicate synthesis processes and efficient multiplex catalyst for the organic pollutant degradation



| | |
|---|---|
| Journal: | *RSC Advances* |
| Manuscript ID | RA-ART-08-2015-016409.R1 |
| Article Type: | Paper |
| Date Submitted by the Author: | 25-Sep-2015 |
| Complete List of Authors: | Hu, Zhong-Ting; Nanyang Technological University, School Civil & Environmental Engineering<br>Lua, Shun Kuang; Nanyang Technological University, School of Materials Science and Engineering<br>Yan, Xiaoli; Nanyang Technological University, School of Civil and Environmental Engineering<br>Lim, Teik-Thye; Nanyang Technological University, Division of Environmental and Water Resources Engineering |
| Subject area & keyword: | |
| | |

RSC Advances

ARTICLE

# Nanostructured hexahedron of bismuth ferrite clusters: Delicate synthesis processes and efficient multiplex catalyst for the organic pollutant degradation

Received 00th January 20xx,
Accepted 00th January 20xx

DOI: 10.1039/x0xx00000x

www.rsc.org/

Zhong-Ting Hu[a]*, Shun Kuang Lua[b], Xiaoli Yan[a,c], Teik-Thye Lim[a]

A novel bismuth ferrite, with the simultaneous formation of nanostructured clusters and controllable morphologies, was fabricated using a delicate synthesis process. Through carefully controlling the entire processes from co-precipitation at a lower temperature in water system to hydrothermal treatment in methanol/water co-solvent system, nanostructured bismuth ferrite clusters with controllable morphologies which are composed of smaller bismuth ferrite crystals (~25 nm) could be obtained. The fast crystal growth of the bismuth ferrites has been successfully hindered and a relatively pure mullite ($Bi_2Fe_4O_9$) structure of the nanostructured bismuth ferrite clusters could be obtained. Their morphologies could be cube-, cuboid- and plate-like shapes with a side length of ~400 nm, a height of ~600 nm and a thickness of ~80 nm, respectively. The resulted nanostructured bismuth ferrite clusters show good crystallinity, uniform elemental distributions, high chemical stability, good dispersity, reusability, and a narrow bandgap of ~2.1 eV. They have remarkable multiplex catalytic activities in the degradation of methyl orange (MO) through visible-light photo-Fenton oxidation, dark Fenton-like reaction and solar photocatalysis. Under visible-light illumination, 99% of MO could be removed in 80 min. Without illumination, 96% of MO could be removed in 4 h. A plausible mechanism of the multiplex catalytic activities is proposed.

## 1. Introduction

Ternary metal oxides, i.e., structures defined as $A_xB_yO_z$ (e.g., $Bi_2Fe_4O_9$, $NiFe_2O_4$, $ZnMn_2O_4$, $CaTiO_3$, $LaCrO_3$, $BiMnO_3$, $Bi_2WO_6$, $CoMoO_4$, etc.), often contain one or more transition-metal elements so that they commonly possess multiple functionalities for various applications.[1-5] Among all ternary mental oxides, bismuth ferrites (BFO) are the promising multiferric materials possessing weak ferromagnetic (FM) and ferroelectric (FE) properties at room temperature.[2, 6, 7] They have three distorted structures with spontaneous polarization, such as perovskite $BiFeO_3$, mullite $Bi_2Fe_4O_9$ and sillenite $Bi_{25}FeO_{40}$.[8-10] Many investigations have revealed that they possess fascinating physical and structural properties and can be applied in ceramic capacitors, ferroelectric memories, information storages, spintronics, sensors and ferroelectric ultrafast optoelectronic devices.[11-15] In recent years, researchers discovered that bismuth ferrites also have fascinating catalysis such as visible-light photocatalysis, acetylation, Fenton-like oxidation etc., which has attracted a great deal of attention.[16-18] More recently, we have reported self-assembled plate-like bismuth ferrites exhibiting remarkable visible-light photo-Fenton oxidation as well as dark Fenton-like reaction and visible-light photocatalysis, suggesting that bismuth ferrites might be useful for degradation of organic pollutants in water treatment through catalytic oxidation processes.[19] Although the catalytic functions of bismuth ferrites were observed, the methods for enhancing their catalytic performance are required. In general, morphology-controllable fabrication is one of the effective approaches for enhancing performance of catalysts, since morphology-controllable nanomaterials (e.g., 1D, 2D, 3D) exhibit enhanced properties compared to their bulk counterparts.[20-23] Much effort has been undertaken to tune the morphology of bismuth ferrites into sheet-, cube-, flower-, octahedron-, rod- and groove-like shapes.[24-30] However, most of the previously synthesized bismuth ferrites were micrometer-sized (≥ 1 μm) morphologies in at least one of their dimensions, and thus they exhibited limited enhanced catalytic activities. To address this problem, development of a novel nanostructured bismuth ferrite could be the overarching strategy.[2] Nanostructured materials have attracted extensive attention, which are distinct from their bulk counterparts and from the atomic or molecular precursors.[31-38] Unfortunately, since bismuth ferrites are sensitive to temperature and oxygen pressure during synthesis, they require careful tuning of synthesis parameters in order to prevent formation of impurity phases.[39-42] Meanwhile, our previous study has demonstrated that bismuth ferrites have the ability of self-assembly with fast crystal

[a] Division of Environmental and Water Resources Engineering, School of Civil and Environmental Engineering, Nanyang Technological University, 50 Nanyang Avenue, Singapore 639798, Singapore. Email: zhu009@ntu.edu.sg
[b] School of Material Science and Engineering, Nanyang Technological University, 50 Nanyang Avenue, Singapore 639798, Singapore
[c] Nanyang Environment & Water Research Institute (NEWRI), Nanyang Technological University, 1 Cleantech Loop, CleanTech One, Singapore 637141, Republic Singapore.

† Footnotes relating to the title and/or authors should appear here.
Electronic Supplementary Information (ESI) available: [details of any supplementary information available should be included here]. See DOI: 10.1039/x0xx00000x

growth.[19] Those are the daunting challenges in synthesis of nanostructured bismuth ferrites.

Here we present a delicate synthesis of nanostructured bismuth ferrites with varied morphologies via combining energy-saving co-precipitation at a lower temperature of 95°C in water system with hydrothermal treatment under mild conditions in methanol/water co-solvent system. The morphologies of bismuth ferrite clusters (i.e., cube-, cuboid- and plate-like shapes) could be tuned by controlling synthesis conditions delicately. The resulting nanostructured bismuth ferrite clusters consist of smaller crystals of 25 nm with grain sizes ranging from 80 to 600 nm in any dimensions. They show good crystallinity, uniform elemental distributions, high chemical stability, good dispersity and reusability as multiplex catalysts. To the best of our knowledge, there has been no report on nanostructured bismuth ferrite clusters with controllable morphologies. A plausible formation mechanism of the nanostructured bismuth ferrite clusters is proposed. The catalytic activity of the nanostructured bismuth ferrite clusters were evaluated for visible-light photo-Fenton oxidation, dark Fenton-like oxidation and solar photocatalysis of methyl orange (MO) as the model pollutant. Finally, a mechanistic insight into depict the multiplex catalytic degradation of a pollutant by the nanostructured bismuth ferrite clusters is proposed.

## 2. Experimental

### 2.1 Materials

Bismuth (III) nitrate pentahydrate (≥ 98%, VWR), ferric (III) nitrate nonahydrate (≥ 99%, Merck), sodium hydroxide (pellet, Schedelco), nitric acid (1N, Merck), citric acid (≥ 99.5%, Merck), urea (99%, Sigma), methanol (LC grade, Merck), absolute ethanol (99.9%, Fisher chemical), methyl orange (85%, Sigma), and hydrogen peroxide (35% w/w, Alfa Aesar) were used in this study. All the chemicals were of analytical grade and used without further purification. Milli-Q ultrapure water (18.2 MΩ cm) was used for all the experiments.

### 2.2 Synthesis of nanostructured bismuth ferrite clusters

Bismuth ferrite clusters with cuboid-like shape were prepared via combining low-temperature co-precipitation with hydrothermal treatment, as illustrated in Fig. 1. Typically, $Bi(NO_3)_3{\cdot}5H_2O$ (1.21 g) and $Fe(NO_3)_3{\cdot}9H_2O$ (2.02 g) were completely dissolved in 2 mL of 2 M $HNO_3$ and citric acid (3.2 g) was dissolved in 5 mL of water, respectively. A transparent solution could be obtained after mixing them together in a Teflon vessel. Then, 33 mL of 12 M NaOH was instantly added into the solution with vigorous stirring. After stirring for 1 h, the Teflon vessel containing the deep-brown slurry was transferred to an oil bath and heated at 95°C with constant stirring. After 12 h, the reaction was cooled down naturally to room temperature. The precipitate was collected and washed using water until pH ~10, followed by re-suspendsed into 6 mL of methanol/water (1:1 v/v) co-solvent by ultrasonication for 10 min. Thereafter, the suspended precipitate was surface-modified by addition of citric acid solution (0.6 g dissolved into 3.5 mL of the co-solvent) to promote its dispersion (noted as "precursor"). Then, 3.82 g of urea was dissolved in 7 mL of the co-solvent at 65°C in water bath, which was then added slowly into the precursor with contineous stirring at room temperature. After 120 min, the dispersion was transferred into a 50-mL Teflon-lined stainless steel autoclave and heated at 200°C for 20 min in an electric oven. After the autoclave reaction chamber was cooled down naturally to room temperature, the product was collected and washed thoroughly with water followed by absolute ethanol. At last, the final product was dried in a vacuum oven at 65°C overnight followed by calcination at 250°C for 1 h under $N_2$ atmosphere to remove the residual citric acid. For comparison, bismuth ferrite clusters with cube-like shape and plate-like shape were also prepared through adjusting the reaction time of the hydrothermal treatment to 10 min and 60 min, respectively.

### 2.3 Characterization

The morphologies and structures of products were investigated using field emission scanning electron microscopy (FESEM, JEOL JSM-7600F) and transmission electron microscopy (TEM, JEOL JEM-2010). The crystal phase was studied through powder X-ray diffraction (XRD) analysis (Bruker, D8 Advance, Cu-Ka, λ = 1.5418 Å). The chemical composition and elemental distribution were examined using Energy Dispersive X-ray (EDX, Oxford Xmax80 LN2 Free) microanalysis. The materials were further characterized using X-ray photoelectron spectroscopy (XPS, Kratos Axis Ultra Spectrometer, Al-Ka at 1486.7 eV, 15 kV voltage, 10 mA emission current) and UV-vis diffuse reflectance spectroscopy (DRS, UV-9000, Metash). The specific surface area was calculated using the Brunauer-Emmet-Teller (BET) equation through $N_2$ adsorption/desorption isotherm (Quantachrome, Quadrasorb SI).

### 2.4 Catalytic evaluation

The catalytic performances of the resulted bismuth ferrite clusters were evaluated through visible-light photo-Fenton oxidation, Fenton-like reaction (dark) and solar photocatalysis, respectively. Methyl orange (MO) is used as the model pollutant because it is quite stable (Fig. S1). Throughout the experimental runs, the pH of the reaction system was rather constant at circumneutral value (~6.5). Typically, the desired amount of the catalyst (0.5 g $L^{-1}$) was added into 50 mL of solution containing 5 mg $L^{-1}$ of MO followed by continuous stirring for 1 h in dark to achieve adsorption/desorption equilibrium. Thereafter, for the visible-light photo-Fenton oxidation experiment, the suspension was added with 1 mmol of $H_2O_2$ (20 mM) and then illuminated with visible light (420-630 nm) using a solar simulator (Newport, 150 W Xenon arc lamp, one sun, polycarbonate filter for UV cut-off). A certain amount of solution was drawn out from the reaction vessel at each designated time interval. After the catalysts were separated, the supernatant solutions were analyzed for UV-vis absorption at ~464 nm using UV-vis spectrometer (SHIMADZU, UV-1800). For the Fenton-like reaction, the experiments were carried out in dark with addition of 3 mmol $H_2O_2$. The reactions for the solar photocatalysis were carried out with solar irradiation from the solar simulator without adding $H_2O_2$.

## 3. Results and discussion

### 3.1 Formation process of nanostructured bismuth ferrite clusters

A plausible evolution of bismuth ferrite clusters with a regular morphology is depicted in Fig. 1. Previous studies from our group have demonstrated that bismuth ferrite has the ability of self-assembled growth.[19] In the present study, citric acid was introduced to control the crystal growth of bismuth ferrites through the induced steric hindrance effect. As shown in Fig. 1 (water system),

Bi/Fe mixed solution (transparent light yellow) will form trinuclear Bi/Fe-citrate complexes (transparent brown) through interaction between citric acid and Bi/Fe ions, followed by transformation to Bi/Fe hydroxides (dark brown) after adding the strong base (NaOH). The resulted hydroxides with abundant citrate surfactants will undergo a dehydration process at a low temperature of 95°C. Due to the steric hindrance effect induced by citrate ions, yellow-brown bismuth ferrite nanoparticles (NPs) without self-assembled growth could be formed (Fig. 1(4)), as revealed by the SEM and XRD analyses (Fig. S2a and b). In order to promote the crystal growth or self-assembled aggregation of bismuth ferrite NPs to form an unique morphology or nanostructure, it is crucial that the citrate-stabilized bismuth ferrite NPs further undergo hydrothermal treatment in the methanol/water co-solvent system. In this treatment process, the effect of the different solvent ratios (methanol/water) on the preparation of bismuth ferrites was investigated as well (Fig S3). As shape-directing agents, the citric acid plays an important role in tuning nanostructured morphologies. As shown in Fig. 1 (co-solvent system), the citrate-stabilized bismuth ferrite NPs will undergo small-group self-assembled aggregation under controlling the amount of citrate surfactants (Fig. 1(5)). Subsequently, in the presence of urea under hydrothermal conditions at 200°C, the aggregated bismuth ferrite NPs can be further reformed into nanoplates (~25 nm) after undergoing crystal dissolution and re-growth processes, while the formed nanoplates tend to aggregate together through subsequent decomposition of citrate surfactants and their self-organization. Finally, unlike previous studies which commonly used hard templates,[43, 44] we obtained the well-suspended deep-yellow bismuth ferrite clusters with a regular morphology under mild conditions in the presence of citrate acid (Fig. 1(6)).

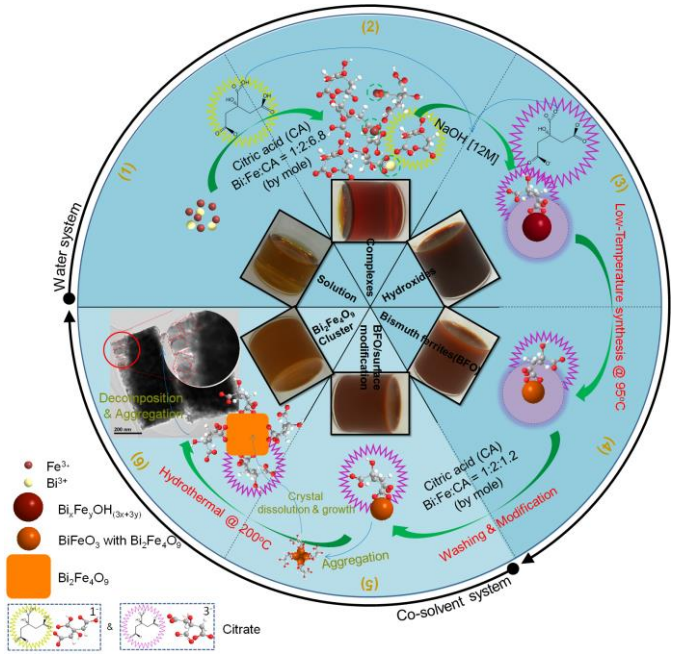


**Fig. 1.** Schematic illustration of the evolution mechanism of cuboid-like nanostructured $Bi_2Fe_4O_9$ clusters through a delicate synthesis included a low-temperature co-precipitation in water system and a hydrothermal treatment in co-solvent system: (1)-(2) formation of Bi/Fe-citrate complexes; (2)-(3) formation of Bi/Fe hydroxide; (3)-(4) formation of bismuth ferrite NPs; (4)-(5) removal of excessive citrate and formation of citrate-stabilized bismuth ferrite NPs; (5)-(6) formation of cuboid-like $Bi_2Fe_4O_9$ clusters.

### 3.2 Characteristics of nanostructured bismuth ferrite clusters

The as-prepared nanostructured bismuth ferrites can form different morphologies through changing the aging time of their hydrothermal treatment with delicate control of the entire synthesis processes (Fig. 2). A plausible reason is that the effect of citrate molecules on the different crystal faces could change during the hydrothermal process, which contributed to the final morphologies/nanostructures of materials.[24, 27] As shown in Fig. 2, the SEM images show three regular morphologies such as "cube-like" (a and b), "cuboid-like" (c and d), and "plate-like" (e and f) shapes. Additional SEM images reveal irregular morphologies when aging time is varied beyond proposed time frame as shown in the Supporting Information (Fig. S4). Fig. 2a and b exhibit well synthesized cube-like bismuth ferrite and its size has the side length of around 400-450 nm. In Fig. 2c and d, a standard cuboid-like morphology has the side length of ~230 nm and height of ~600 nm with great uniformity and narrow size distribution. In Fig. 2e and f, the morphology of bismuth ferrites displays a square plate-like shape. This structure has the typical length of ~380 nm and thickness of ~80 nm. Moreover, it seems that bismuth ferrites with regular morphologies are composed of subunits (Fig. 2b, d and f). For the detailed information, further investigations were carried out via transmission electron microscopy (TEM).

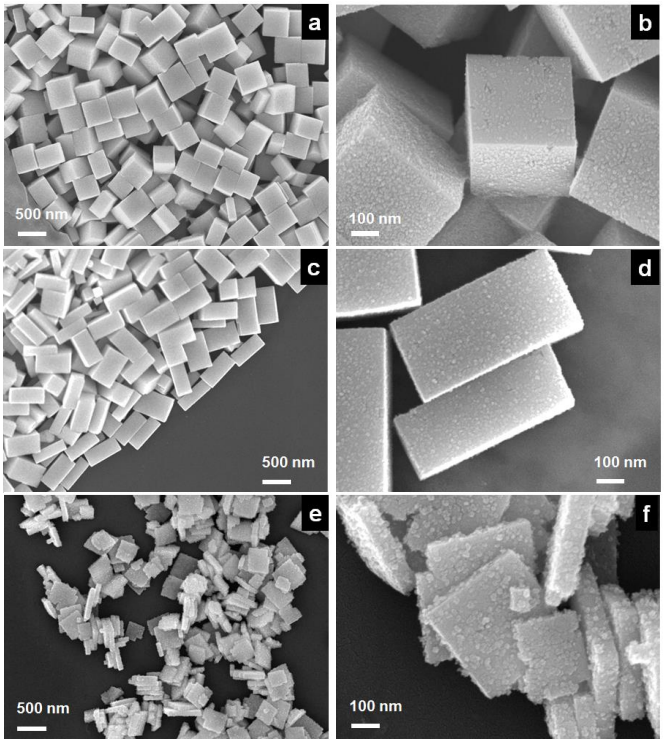


Fig. 2. SEM images of nanostructured bismuth ferrite clusters with different morphologies of cube-like (a and b), cuboid-like (c and d) and plate-like (e and f) shapes.

The corresponding TEM images further confirm the morphologies for the as-prepared bismuth ferrites (Fig. 3). In addition, the TEM images display a strong mass-thickness contrast observed as the dark and light within the as-prepared samples, implying that the as-prepared bismuth ferrites with regular morphologies are consisted of smaller units (crystals). The selected area electron diffraction (SAED) patterns of the as-prepared samples are shown in Fig. 3 (inset). The SAED patterns reveal that the as-prepared bismuth ferrites are the poly-crystalline materials, indicating the obtained bismuth ferrites with different morphologies are present as

clusters. The as-prepared bismuth ferrite clusters with nanostructured cube-like, cuboid-like and plated-like morphologies are hereafter referred as NSC-$Bi_2Fe_4O_9$, NSCC-$Bi_2Fe_4O_9$ and NSP-$Bi_2Fe_4O_9$, respectively.

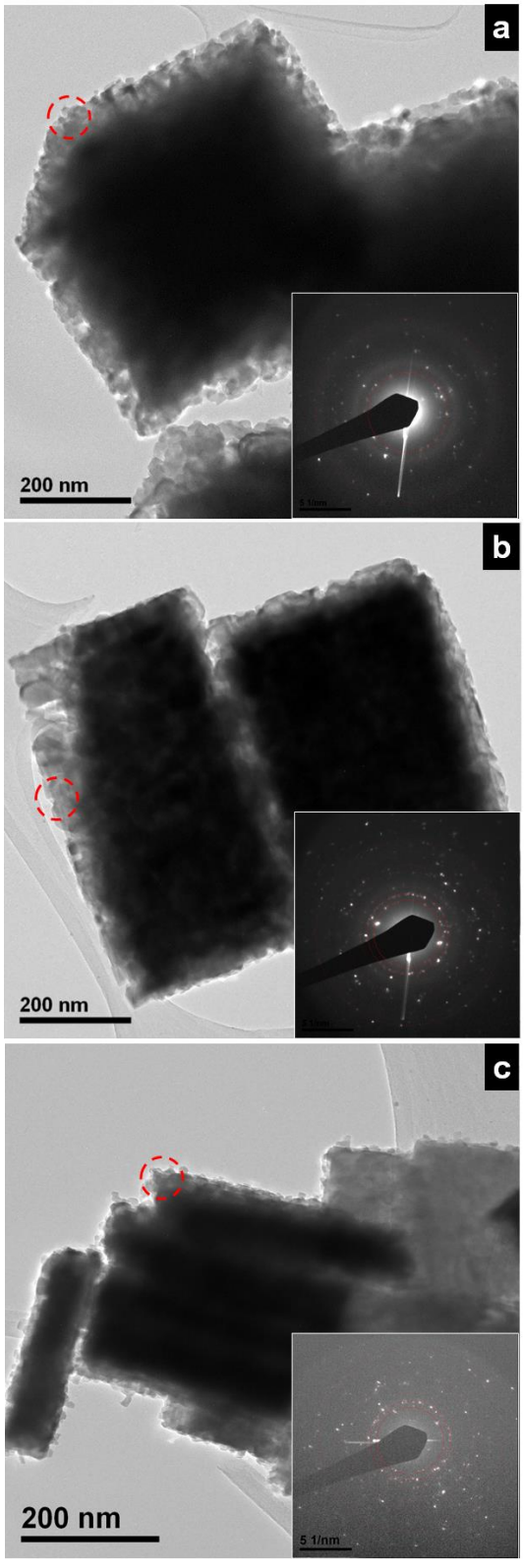


Fig. 3. TEM images and corresponding SAED patterns (inset) for nanostructured bimuth ferrite clusters of cube-like (a), cuboid-like (b) and plate-like (c) shapes.

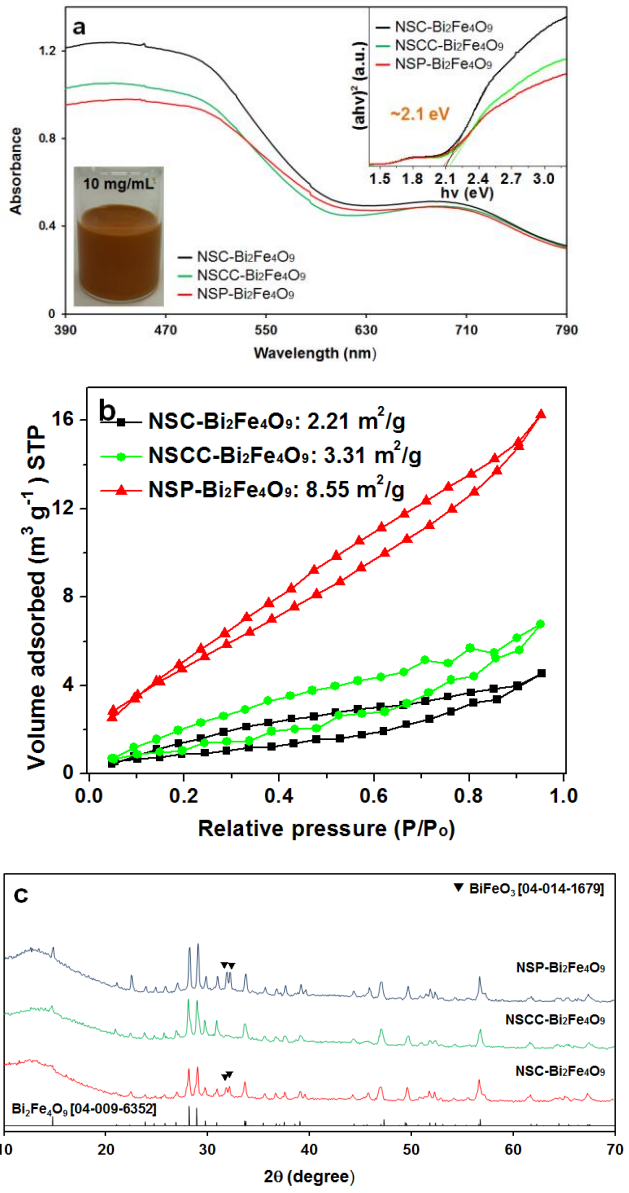


Fig. 4. (a) UV-vis absorption spectra and Kubelka-Munk transformed reflectance spectra of NSC-$Bi_2Fe_4O_9$, NSCC-$Bi_2Fe_4O_9$ and NSP-$Bi_2Fe_4O_9$ samples, and the representative well suspension of nanostructured bismuth ferrite clusters (NSCC-$Bi_2Fe_4O_9$) in ethanol/water co-solvent. (b) Nitrogen adsorption/desorption isotherms, and (c) XRD patterns of NSC-$Bi_2Fe_4O_9$, NSCC-$Bi_2Fe_4O_9$ and NSP-$Bi_2Fe_4O_9$ samples.

The optical properties of bismuth ferrite clusters were investigated by using UV-vis diffuse reflectance spectroscopy (DRS). As shown in Fig. 4a (inset), well-suspended bismuth ferrites in ethanol/water (1:1 v/v) co-solvent exhibit deep-yellow color. The color of the as-prepared sample implies that bismuth ferrite clusters have the capability of visible light absorption. Additionally, Fig. 4a displays that the as-prepared samples (i.e., NSC-$Bi_2Fe_4O_9$, NSCC-$Bi_2Fe_4O_9$ and NSP-$Bi_2Fe_4O_9$) exhibit similar photo-absorption abilities in the visible-light region from 400 to 700 nm. It further confirmed that bismuth ferrite clusters have a remarkable light absorption in the visible-light region. The corresponding optical bandgaps are calculated by the Kubelka-Munk function shown in Fig. 4a (inset). The results show that the as-prepared samples have a similar optical bandgap about 2.1 eV, implying that bismuth ferrite clusters can function as visible-light photocatalysts. In addition, the optical

bandgap for bismuth ferrite can be narrowed to ~1.82 eV (Fig. S2c). The above results indicate that nanostructured bismuth ferrite clusters with various morphologies have remarkable photoresponse properties under visible light irradiation. On the other hand, the surface areas of the as-prepared samples (i.e., NSC-$Bi_2Fe_4O_9$, NSCC-$Bi_2Fe_4O_9$ and NSP-$Bi_2Fe_4O_9$) were investigated using nitrogen adsorption-desorption measurements (Fig. 4b). All three samples exhibit type III isotherms with a hysteresis loop in the relative pressure. The corresponding BET surface areas are 2.21, 3.31 and 8.55 $m^2 g^{-1}$, respectively. The surface area of the NSP-$Bi_2Fe_4O_9$ sample (8.55 $m^2 g^{-1}$) is larger than that of the bulk (0.53 $m^2 g^{-1}$) and flower-like (4.3 $m^2 g^{-1}$) bismuth ferrites.[26, 45]

The crystalline phases of bismuth ferrite clusters were confirmed by XRD analysis. As shown in Fig. 4c, the XRD patterns of the as-prepared NSC-$Bi_2Fe_4O_9$, NSCC-$Bi_2Fe_4O_9$ and NSP-$Bi_2Fe_4O_9$ samples with high intensities of diffraction peaks indicate that the as-prepared bismuth ferrite clusters all are ternary bismuth ferrites with high crystallinity. They are mainly composed of mullite bismuth ferrites ($Bi_2Fe_4O_9$, JCPDS PDF 04-009-6352).[9] In particular, the NSC-$Bi_2Fe_4O_9$ and NSP-$Bi_2Fe_4O_9$ samples also contained a small fraction of perovskite bismuth ferrites ($BiFeO_3$, JCPDS PDF 04-014-1679).[8] It is estimated by Rietveld analysis that the perovskite bismuth ferrites were present at the percentages of 7.04, 1.28 and 9.40% in NSC-$Bi_2Fe_4O_9$, NSCC-$Bi_2Fe_4O_9$ and NSP-$Bi_2Fe_4O_9$ samples respectively (TOPAS V4.1). Nevertheless, all of them have no observable characteristic diffraction peaks corresponding to sillenite bismuth ferrites ($Bi_{25}FeO_{40}$, JCPDS PDF 01-073-9538).[46] Moreover, there are no obvious evidences of impurities such as separated phases, i.e., $Bi_2O_3$ (01-074-2351),[47] hematite $Fe_2O_3$ (01-088-2359)[48] and magnetite $Fe_3O_4$ (04-009-8443).[49] The phase purity analysis of bismuth ferrites has already been discussed in detail in previous reports.[19, 50] Without the hydrothermal treatment, the composition for crystalline phases of bismuth ferrites becomes different. As compared with the samples treated with hydrothermal, bismuth ferrites are mainly consisted of perovskite bismuth ferrites (Fig. S2b). In order to obtain mullite bismuth ferrites, the conventional calcination method was carried out by adjusting temperatures and holding times before we used this reported hydrothermal method as the post-treatment. Relatively pure mullite bismuth ferrites could be prepared via calcination at 700°C (Fig. S5a). Meanwhile, there is the minor effect of the holding time on synthesis of mullite bismuth ferrites using a longer reaction time when the temperature was controlled under 700°C (Fig. S5b). However, the prepared mullite bismuth ferrites have the poor morphology and particle size distribution with micro-scaled sizes (Fig. S5c). Besides, a relatively pure mullite bismuth ferrite could not be formed when the holding time was decreased to 20 min (see Fig. S5b, there is coexisting perovskite bismuth ferrites). In contrast to the above results, there is clear indication that the proposed hydrothermal treatment is beneficial to produce mullite bismuth ferrites with nano-scaled sizes under mild conditions. However, it must be treated with respectful caution using hydrothermal treatment because bismuth ferrite as a ternary oxide is changeable easily between its different crystalline phases[51]. As shown in Fig. 4c, the relative pure bismuth ferrite (i.e., the NSCC-$Bi_2Fe_4O_9$ sample) could be obtained in well-controlled conditions in which the aging time of hydrothermal treatment should be arranged between 10 to 60 min under this delicate synthesis process.

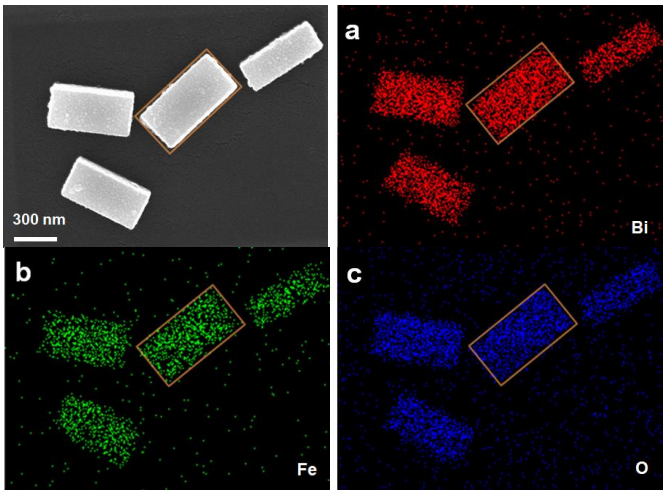


Fig. 5. (a) SEM image of NSCC-$Bi_2Fe_4O_9$ sample and the corresponding EDX elemental distribution mappings of Bi (a1), Fe (a1) and O (a3).

The properties of bismuth ferrite clusters were further investigated by energy dispersive X-ray (EDX) microanalysis and X-ray photoelectron spectroscopy (XPS) analyses. Fig. 5 shows the EDX elemental distribution mappings of Bi, Fe and O within the NSCC-$Bi_2Fe_4O_9$ sample. As compared with the appropriate SEM image of NSCC-$Bi_2Fe_4O_9$, it clearly shows that the elemental distributions of Bi, Fe and O within the as-prepared bismuth ferrite clusters (i.e., NSCC-$Bi_2Fe_4O_9$) are uniform. It was further confirmed through the EDX analysis of the NSC-$Bi_2Fe_4O_9$ sample (Fig. S6). The EDX analysis indicates a high degree of uniformity in elemental distributions for the nanostructured bismuth ferrite cluster, and implies that nanostructured bismuth ferrite clusters with different morphologies could be produced using our creative synthesis processes.

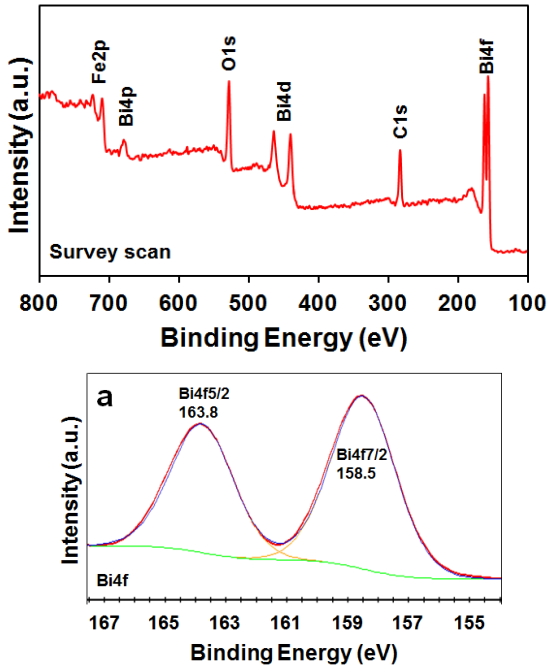

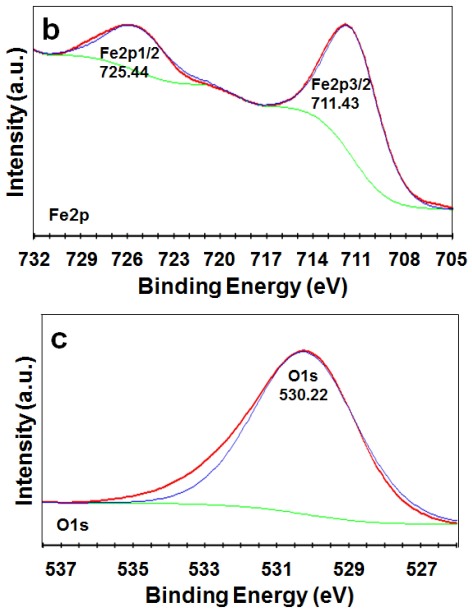


**Fig. 6.** XPS survey scan spectra of NSCC-$Bi_2Fe_4O_9$ sample and its high resolution spectra of Bi4f (a), Fe2p (b) and O1s (c).

Fig. 6 exhibits the full XPS spectra of the as-prepared bismuth ferrite clusters (NSCC-$Bi_2Fe_4O_9$). It is clearly shown that all the standard photoelectron peaks of the NSCC-$Bi_2Fe_4O_9$ sample, i.e., Fe2p, Bi4p, O1s, Bi4d, C1s and Bi4f, are presented. These results match well with that of the EDX analysis in which the C1s peak probably come from the residual carbon in the organic compound. High resolution spectra of Bi4f, Fe2p and O1s are shown in Fig. 6a-c. The Thermo Advantage V5.945 is used to analyse XPS deconvolution. The characteristic peaks of Bi4f5/2 and Bi4f7/2 at ~163.8 eV and ~158.5 eV (Fig. 6a) are attributed to the spin-orbit splitting of the Bi4f components, which are in good agreement with the $Bi^{3+}$ species. Fig. 6b presents the characteristic peaks of Fe2p such as Fe2p1/2 (~725.44 eV) and Fe2p3/2 (~711.43 eV), corresponding to $Fe^{3+}$ species. There are no obvious reduced states of Fe such as $Fe^{2+}$ and $Fe^0$. Moreover, the as-prepared nanostructured bismuth ferrite clusters show that the characteristic peak of O1s is located at ~530.22 eV, which can be attributed to the O1s binding energy of $O^{2-}$ in the lattice. All of them are consistent with the reported literatures previously.[28, 52, 53]

### 3.3 Performance of nanostructured bismuth ferrite clusters in degradation of MO

Heterogeneous catalysis is beneficial for catalyst separation and recovery, thus avoiding contribution as the secondary pollutants in the treated water, but commonly the degradation efficiency of heterogeneous catalysis is relatively weaker.[54, 55] Moreover, a novel catalyst, which can drive multiplex catalytic activities, is required in water treatment. Herein, the as-prepared nanostructured bismuth ferrite clusters exhibit high performances with multiplex catalytic activities in heterogeneous visible-light photo-Fenton oxidation, Fenton-like reaction in the dark and solar photocatalysis. The corresponding investigations on the degradation of organic pollutants were carried out at pH ~6.5. Fig. 7a shows the degradation of MO as a function of irradiation time with the three as-prepared samples in the presence of $H_2O_2$ and visible-light illumination (420-630 nm). In the absence of the catalysts, the degradation of MO is insignificant (< 3% over 3 h) even with $H_2O_2$ addition and visible-light illumination. In contrast, a rapid decrease in the concentration of MO was observed in the presence of the catalysts (i.e., NSC-$Bi_2Fe_4O_9$, NSCC-$Bi_2Fe_4O_9$ and NSP-$Bi_2Fe_4O_9$), indicating that nanostructured bismuth ferrite clusters can effectively promote visible-light photo-Fenton oxidation. Fig. 7a (inset) displays the discoloring of MO solution as the reaction proceeds in the presence of the NSP-$Bi_2Fe_4O_9$ sample and $H_2O_2$, suggesting that the chromophoric structure of MO was decomposed already (the corresponding changes of temporal absorption spectra of the MO solution are shown in Fig. S7). The degradation efficiencies of MO in 80 min and the corresponding apparent degradation rate constants ($k_{app}$) are summarized in Table 1. Typically, the kinetics of the degradation process follows a pseudo-first-order kinetic model, $\ln(C/C_o) = -k_{app}t$, where $k_{app}$ is the apparent degradation rate constant, $C_o$ and C are the concentration of MO at initial and at a certain reaction time t, respectively. As shown in Table 1, the degradation efficiencies of MO reach 92, 99 and 99% for the as-prepared NSC-$Bi_2Fe_4O_9$, NSCC-$Bi_2Fe_4O_9$ and NSP-$Bi_2Fe_4O_9$ samples, individually. According to the corresponding $k_{app}$ values, the catalytic activities for visible-light photo-Fenton oxidation are significantly influenced by the morphologies in the order of NSP-$Bi_2Fe_4O_9$ > NSCC-$Bi_2Fe_4O_9$ > NSC-$Bi_2Fe_4O_9$.

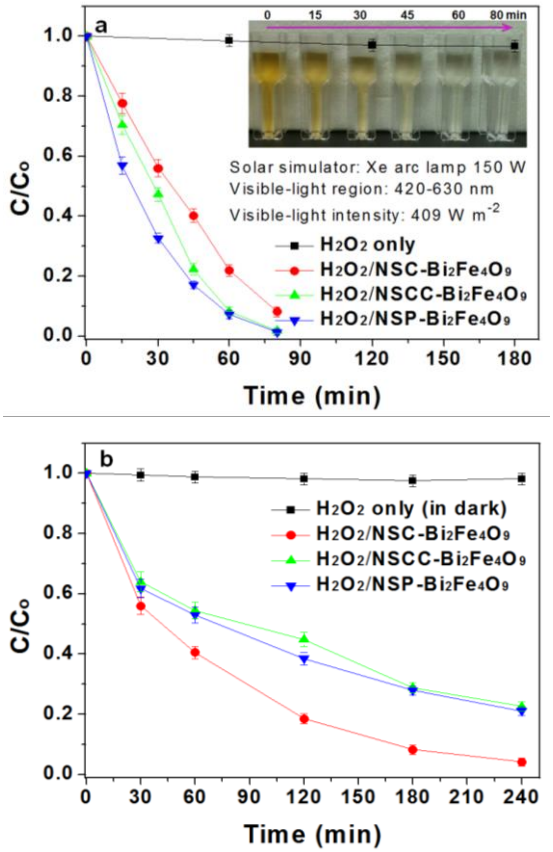

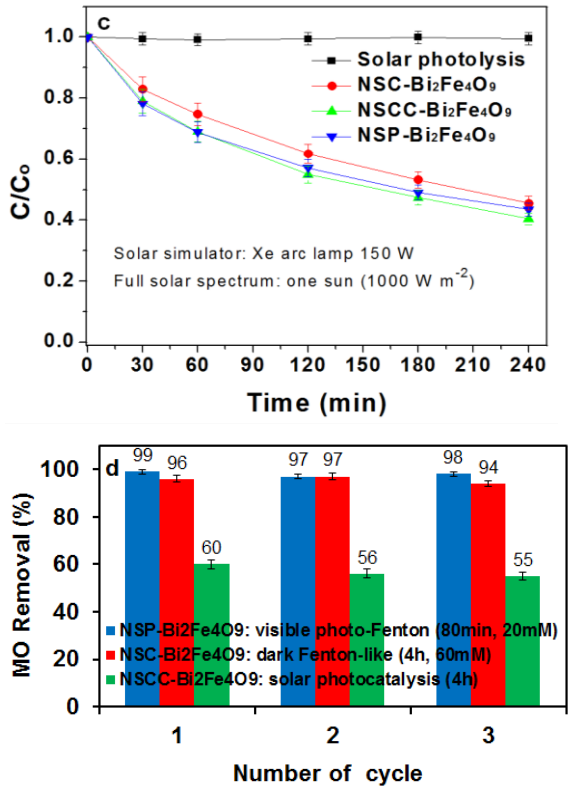


**Fig. 7.** Performance of nanostructured bismuth ferrite clusters for degradation of MO through (a) visible-light photo-Fenton oxidation, (b) dark Fenton-like oxidation and (c) solar photocatalysis. (d) Efficiency of reused nanostructured bismuth ferrite clusters in degradation of MO through different catalytic oxidation processes.

Fig. 7b shows the degradation of MO through heterogeneous Fenton-like reaction in the dark. As shown in the figure, the degradation efficiency of MO is insignificant (≤ 2% in 4 h) even with $H_2O_2$ addition when there is an absence of nanostructured bismuth ferrite clusters. In contrast, a rapid decrease in the concentration of MO was observed in the presence of the nanostructured bismuth ferrite clusters. The degradation efficiencies of MO are 96, 77 and 78% for the Fenton-like reaction with NSC-$Bi_2Fe_4O_9$, NSCC-$Bi_2Fe_4O_9$ and NSP-$Bi_2Fe_4O_9$, respectively (Table 1). These results demonstrate that the nanostructured bismuth ferrite clusters exhibit remarkable catalytic performance in Fenton-like reaction even at pH ~6.5, and it will be more economical and eco-friendly than that of traditional Fenton/Fenton-like catalysis at pH ≤ 3 through application of the nanostructured bismuth ferrite clusters into the water treatment at circumneutral pH values. Furthermore, we also investigated the semiconductor photocatalytic activity of the nanostructured bismuth ferrite clusters. Fig. 7c shows that the degradation efficiency of MO can be negligible (≤ 0.5%) in the absence of the catalysts through solar photolysis. In contrast, with the presence of the NSC-$Bi_2Fe_4O_9$, NSCC-$Bi_2Fe_4O_9$ and NSP-$Bi_2Fe_4O_9$, 54, 60 and 56% of MO could be degraded, respectively. The results suggest that the photocatalytic activities for the nanostructured bismuth ferrite clusters with various morphologies are similar.

Chemical stability of a catalyst is important for its practical application. The corresponding investigation was carried out and the results show that the nanostructured bismuth ferrite clusters exhibit good reusability potential (Fig. 7d). The slight reduction in the efficiencies of the degradation of MO might be due to the residual MO (or by-products) accumulation on the catalyst surface. The reaction solutions were also analyzed with inductively coupled plasma-optical emission spectrometer (ICP-OES, Perkin Elmer Optima 2000DV) during the processes of visible-light photo-Fenton oxidation, dark Fenton-like reaction and solar photocatalysis. The results display that the concentrations of the ion species (i.e., $Bi^{3+}$, $Fe^{3+}/Fe^{2+}$) are quite low (< 0.1 mg $L^{-1}$ or corresponding to < 0.02% (w/w) in the added amount of catalysts). The above results indicate that the as-prepared bismuth ferrite clusters have good chemical stability and reusability.

### 3.4 Proposed mechanism

Fig. 8 illustrates a plausible mechanism of catalytic degradation of organic pollutants by the nanostructured bismuth ferrite clusters. The interconversion between Fe(III) and Fe(II) takes place internally within nanostructured bismuth ferrite clusters along with both formation of reactive oxygen species (ROSs) and consumption of $H_2O_2$. Without solar illumination (night time), ROSs such as $HO_2^{\cdot}$ and $OH^{\cdot}$ were formed in which the reaction pathway can be described by Eqs (1)-(2).

$Bi_2Fe_4O_9(Fe(III)) + H_2O_2 \rightarrow Bi_2Fe_4O_9(Fe(II)) + H^+ + HO_2^{\cdot}$ (1)

$Bi_2Fe_4O_9(Fe(III)) + H_2O_2 \leftrightarrow Bi_2Fe_4O_9(Fe(III))(HO_2^-) + H^+$ (0.001-0.01 $M^{-1} S^{-1}$) (1a)

$Bi_2Fe_4O_9(Fe(III))(HO_2^-) \rightarrow Bi_2Fe_4O_9(Fe(II)) + HO_2^{\cdot}$ (70 $M^{-1} S^{-1}$) (1b)

$Bi_2Fe_4O_9(Fe(II)) + H_2O_2 \rightarrow Bi_2Fe_4O_9(Fe(III)) + OH^- + HO^{\cdot}$ (2)

The reaction as shown by the dashed-dotted blue line has a lower reaction rate constant because of the rate-limiting step (Eq (1a)) with a reaction rate constant of 0.001-0.01 $M^{-1} S^{-1}$.[56, 57] Nevertheless, $OH^{\cdot}$ instead of the $HO_2^{\cdot}$ will be formed under solar illumination (day time). This reaction pathway (Eq (3)) is shown below:

$Bi_2Fe_4O_9(Fe(III)) + 2H_2O_2 + hv\ (\lambda > 420nm) \rightarrow Bi_2Fe_4O_9(Fe(II)) + HO^{\cdot} + H^+ + H_2O + O_2$ (3)

It is defined as photo-Fenton oxidation, which can be successfully excited under visible light irradiation and effectively enhance the interconversion between Fe(III) and Fe(II) along with the abundant formation of $OH^{\cdot}$.[19, 58-60] Meanwhile, the photogenerated electrons and holes of nanostructured bismuth ferrite clusters are formed followed by charge migration to the surface of catalyst. Typically, the electrons will react with the adsorbed $O_2$ to form $O_2^{\cdot-}$ and further transform to autogenerated $H_2O_2$ and $OH^{\cdot}$, while the holes are utilized to form autogenerated $O_2$.[19, 61] The corresponding reactions are shown in Eqs (4)-(10).

$Bi_2Fe_4O_9 + hv\ (\lambda > 420nm) \rightarrow h^+ + e^-$ (4)

$e^- + O_2 \rightarrow O_2^{\cdot-}$ (5)

$4h^+ + H_2O \rightarrow 4H^+ + O_2$ (6)

$O_2^{\cdot-} + H^+ \leftrightarrow HO_2^{\cdot}$ (7)

$HO_2^{\cdot} + HO_2^{\cdot} \rightarrow H_2O_2 + O_2$ (8)

$(or\ O_2^{\cdot-} + e^- + 2H^+ \rightarrow H_2O_2)$ (9)

$H_2O_2 + e^- + H^+ \rightarrow HO^{\cdot} + H_2O$ (10)

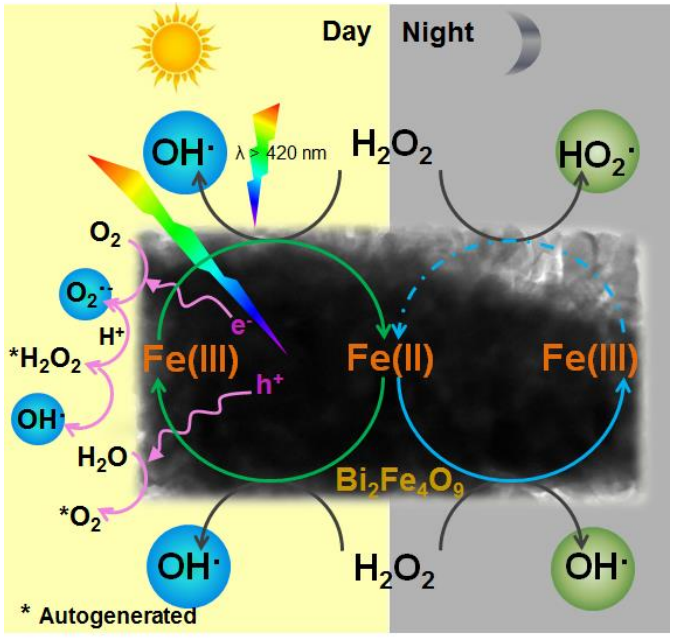


**Fig. 8.** Schematic illustration of multiplex catalytic activities for nanostructured bismuth ferrite clusters.

## 4. Conclusions

In summary, we have developed a delicate approach combining co-precipitation at a lower temperature in water system with hydrothermal treatment under mild conditions in methanol/water co-solvent system for synthesis of novel nanostructured bismuth ferrite clusters with controllable morphologies (i.e., cube-, cuboid-, plate-like). In the present study, this technique has successfully hindered the fast crystal growth of the bismuth ferrites. The aging time of hydrothermal treatment has a significant effect on both the resulting morphology and the crystalline phases of the nanostructured bismuth ferrite clusters. We also successfully obtained the pure mullite ($Bi_2Fe_4O_9$) structure of the nanostructured bismuth ferrite clusters. The resulted nanostructured bismuth ferrite clusters exhibit good crystallinity, uniform elemental distributions, high chemical stability, good dispersity and reusability. Besides, they have remarkable multiplex catalytic activities in the degradation of organic pollutants. Hence, there is significant potential for the application of nanostructured bismuth ferrite clusters in environmental pollution control as well as other fields.

## Acknowledgements

The authors would like to thank Nanyang Technological University (NTU) for the award of a PhD research scholarship and all the laboratory staffs for their kind assistance who come from Central Environmental Science and Engineering Laboratory (CESEL) and FACTS (Facility for Analysis, Characterisation Testing and Simulation).

## Notes and references

1. D. R. Modeshia and R. I. Walton, *Chemical Society Reviews*, 2010, **39**, 4303-4325.
2. Y. Mao, T. J. Park and S. S. Wong, *Chemical Communications*, 2005, 5721-5735.
3. D. Kang, Y. Park, J. C. Hill and K.-S. Choi, *The Journal of Physical Chemistry Letters*, 2014, **5**, 2994-2999.
4. H. Yu, C. Guan, X. Rui, B. Ouyang, B. Yadian, Y. Huang, H. Zhang, H. E. Hoster, H. J. Fan and Q. Yan, *Nanoscale*, 2014, **6**, 10556-10561.
5. N. Zhang, R. Ciriminna, M. Pagliaro and Y.-J. Xu, *Chemical Society Reviews*, 2014, **43**, 5276-5287.
6. S.-W. Cheong and M. Mostovoy, *Nat Mater*, 2007, **6**, 13-20.
7. A. Filippetti and N. A. Hill, *Physical Review B*, 2002, **65**, 195120.
8. P. Ravindran, R. Vidya, A. Kjekshus, H. Fjellvåg and O. Eriksson, *Physical Review B*, 2006, **74**, 224412.
9. E. Kostiner and G. L. Shoemaker, *Journal of Solid State Chemistry*, 1971, **3**, 186-189.
10. A. Friedrich, E. A. Juarez-Arellano, E. Haussühl, R. Boehler, B. Winkler, L. Wiehl, W. Morgenroth, M. Burianek and M. Mühlberg, *Acta Crystallographica Section B: Structural Science*, 2010, **66**, 323-337.
11. N. Hur, S. Park, P. A. Sharma, J. S. Ahn, S. Guha and S. W. Cheong, *Nature*, 2004, **429**, 392-395.
12. J. Wang, J. B. Neaton, H. Zheng, V. Nagarajan, S. B. Ogale, B. Liu, D. Viehland, V. Vaithyanathan, D. G. Schlom, U. V. Waghmare, N. A. Spaldin, K. M. Rabe, M. Wuttig and R. Ramesh, *Science*, 2003, **299**, 1719-1722.
13. T. Kimura, T. Goto, H. Shintani, K. Ishizaka, T. Arima and Y. Tokura, *Nature*, 2003, **426**, 55-58.
14. M. E. Lines and A. M. Glass, *Principles and applications of ferroelectrics and related materials*, Clarendon press Oxford, 2001.
15. K. Takahashi, N. Kida and M. Tonouchi, *Physical review letters*, 2006, **96**, 117402.
16. W. Luo, L. Zhu, N. Wang, H. Tang, M. Cao and Y. She, *Environmental science & technology*, 2010, **44**, 1786-1791.
17. Y. Sun, X. Xiong, Z. Xia, H. Liu, Y. Zhou, M. Luo and C. Wang, *Ceramics International*, 2013, **39**, 4651-4656.
18. C. J. Tsai, C. Y. Yang, Y. C. Liao and Y. L. Chueh, *Journal of Materials Chemistry*, 2012, **22**, 17432-17436.
19. Z.-T. Hu, B. Chen and T.-T. Lim, *RSC Advances*, 2014, **4**, 27820-27829.
20. J. T. Han, Y. H. Huang, X. J. Wu, C. L. Wu, W. Wei, B. Peng, W. Huang and J. B. Goodenough, *Advanced Materials*, 2006, **18**, 2145-2148.
21. B. Wang, H. Wu, L. Yu, R. Xu, T. T. Lim and X. W. Lou, *Advanced Materials*, 2012, **24**, 1111-1116.
22. Q.-J. Ruan and W.-D. Zhang, *The Journal of Physical Chemistry C*, 2009, **113**, 4168-4173.
23. S. Li, Y. H. Lin, B. P. Zhang, Y. Wang and C. W. Nan, *Journal of Physical Chemistry C*, 2010, **114**, 2903-2908.
24. X. Zhang, L. Bourgeois, J. Yao, H. Wang and P. A. Webley, *Small*, 2007, **3**, 1523-1528.
25. U. A. Joshi, J. S. Jang, P. H. Borse and J. S. Lee, *Applied Physics Letters*, 2008, **92**, 242106.
26. S. Sun, W. Wang, L. Zhang and M. Shang, *The Journal of Physical Chemistry C*, 2009, **113**, 12826-12831.
27. X.-Z. Chen, Z.-C. Qiu, J.-P. Zhou, G. Zhu, X.-B. Bian and P. Liu, *Materials Chemistry and Physics*, 2011, **126**, 560-567.
28. A. Sun, H. Chen, C. Song, F. Jiang, X. Wang and Y. Fu, *RSC Advances*, 2013, **3**, 4332-4340.

29. K. Chybczyńska, P. Ławniczak, B. Hilczer, B. Łęska, R. Pankiewicz, A. Pietraszko, L. Kępiński, T. Kałuski, P. Cieluch, F. Matelski and B. Andrzejewski, *Journal of Materials Science*, 2014, **49**, 2596-2604.
30. Y. Liu, R. Zuo and S. Qi, *Powder Technology*, 2014, **254**, 30-35.
31. J. B. Joo, Q. Zhang, I. Lee, M. Dahl, F. Zaera and Y. Yin, *Advanced Functional Materials*, 2012, **22**, 166-174.
32. J. Liu, S. Z. Qiao, Q. H. Hu and G. Q. Lu, *Small*, 2011, **7**, 425-443.
33. Z. Lu, C. Gao, Q. Zhang, M. Chi, J. Y. Howe and Y. Yin, *Nano Letters*, 2011, **11**, 3404-3412.
34. A. S. Edelstein and R. Cammaratra, *Nanomaterials: synthesis, properties and applications*, CRC Press, 1998.
35. P. Yang, *The chemistry of nanostructured materials*, World Scientific, 2011.
36. S. Mann and G. A. Ozin, *Nature*, 1996, **382**, 313-318.
37. M. A. El-Sayed, *Accounts of chemical research*, 2004, **37**, 326-333.
38. F. Gao, X. Y. Chen, K. B. Yin, S. Dong, Z. F. Ren, F. Yuan, T. Yu, Z. G. Zou and J. M. Liu, *Advanced Materials*, 2007, **19**, 2889-2892.
39. P. Fischer, M. Polomska, I. Sosnowska and M. Szymanski, *Journal of Physics C*, 1980, **13**, 1931.
40. J. L. Mukherjee and F. F. Y. Wang, *Journal of the American Ceramic Society*, 1971, **54**, 31-34.
41. M. M. Murshed, G. Nénert, M. Burianek, L. Robben, M. Mühlberg, H. Schneider, R. X. Fischer and T. M. Gesing, *Journal of Solid State Chemistry*, 2013, **197**, 370-378.
42. R. Safi and H. Shokrollahi, *Progress in Solid State Chemistry*, 2012, **40**, 6-15.
43. Y. Liu, J. Goebl and Y. Yin, *Chemical Society Reviews*, 2013, **42**, 2610-2653.
44. L. Vigderman, B. P. Khanal and E. R. Zubarev, *Advanced Materials*, 2012, **24**, 4811-4841.
45. T.-J. Park, G. C. Papaefthymiou, A. R. Moodenbaugh, Y. Mao and S. S. Wong, *Journal of Materials Chemistry*, 2005, **15**, 2099-2105.
46. C. E. Infante and B. Carrasco, *Materials Letters*, 1986, **4**, 194-197.
47. G. Gattow and D. Schutze, Zeitschrift fur Anorganische and Allgemeine Chemie, 1964, 328, 44-68.
48. M. Catti, G. Valerio and R. Dovesi, *Physical Review B*, 1995, **51**, 7441-7450.
49. H. Okudera, K. Kihara and T. Matsumoto, *Acta Crystallographica Section B: Structural Science*, 1996, **52**, 450-457.
50. Z.-T. Hu, J. Liu, X. Yan, W.-D. Oh and T.-T. Lim, *Chemical Engineering Journal*, 2015, **262**, 1022-1032.
51. G. Catalan and J. F. Scott, *Advanced Materials*, 2009, **21**, 2463-2485.
52. J. An, L. Zhu, N. Wang, Z. Song, Z. Yang, D. Du and H. Tang, *Chemical Engineering Journal*, 2013, **219**, 225-237.
53. J. Wu, S. Mao, Z.-G. Ye, Z. Xie and L. Zheng, *Journal of Materials Chemistry*, 2010, **20**, 6512-6516.
54. M. B. Gawande, P. S. Branco and R. S. Varma, *Chemical Society Reviews*, 2013, **42**, 3371-3393.
55. C. Costentin, M. Robert and J. M. Savéant, *Chemical Society Reviews*, 2013, **42**, 2423-2436.
56. C. Walling and A. Goosen, *Journal of the American Chemical Society*, 1973, **95**, 2987-2991.
57. T. Rigg, W. Taylor and J. Weiss, *The Journal of Chemical Physics*, 1954, **22**, 575-577.
58. W. H. Koppenol, J. Butler and J. W. v. Leeuwen, *Photochemistry and Photobiology*, 1978, **28**, 655-658.
59. J. J. Pignatello, *Environmental Science & Technology*, 1992, **26**, 944-951.
60. J. J. Pignatello, D. Liu and P. Huston, *Environmental Science & Technology*, 1999, **33**, 1832-1839.
61. A. Fujishima and X. Zhang, *Comptes Rendus Chimie*, 2006, **9**, 750-760.

RSC Advances

ARTICLE

**Table 1** Kinetic constants and removal efficiencies using nanostructured bismuth ferrites at various catalytic oxidation processes

| AOPs | Photo-Fenton oxidation (visible) | | | Fenton-like reaction (dark) | | | Solar photocatalysis | | |
|---|---|---|---|---|---|---|---|---|---|
| Sample | Removal (%)[a] | $k_{app}$ ($\times 10^{-3}$ $min^{-1}$) | $R^2$ | Removal (%)[b] | $k_{app}$ ($\times 10^{-3}$ $min^{-1}$) | $R^2$ | Removal (%)[b] | $k_{app}$ ($\times 10^{-3}$ $min^{-1}$) | $R^2$ |
| NSC-$Bi_2Fe_4O_9$ | 92 | 22.7 | 0.981 | 96 | 13.6 | 0.997 | 54 | 3.5 | 0.982 |
| NSCC-$Bi_2Fe_4O_9$ | 99 | 36.2 | 0.963 | 77 | 6.7 | 0.971 | 60 | 4.2 | 0.972 |
| NSP-$Bi_2Fe_4O_9$ | 99 | 41.2 | 0.995 | 78 | 7.1 | 0.968 | 56 | 3.9 | 0.961 |

[a] Removal rate of MO at 80 min.
[b] Removal rate of MO at 240 min.

RSC Advances

ARTICLE